Exploring topological transport in Pt_2HgSe_3 nanoribbons: Insights for spintronic device integration

Rafael L. H. Freire [1,*] F. Crasto de Lima [1,†] Roberto H. Miwa,[2,‡] and A. Fazzio[1,§]

[1]*Ilum School of Science, Brazilian Center for Research in Energy and Materials (CNPEM), 13083-100 Campinas, São Paulo, Brazil*

[2]*Instituto de Física, Universidade Federal de Uberlândia, 38400-902 Uberlândia, Minas Gerais, Brazil*

(Received 10 May 2024; revised 13 June 2024; accepted 17 June 2024; published 2 July 2024)

The discovery of the quantum spin Hall effect led to the exploration of the electronic transport for spintronic devices. We theoretically investigated the electronic conductance in large-gap realistic quantum spin Hall system Pt_2HgSe_3 nanoribbons. By an *ab initio* approach, we found that the edge states present a penetration depth of about 0.9 nm, much smaller than those predicted in other two-dimensional topological systems, thus, suggesting that Pt_2HgSe_3 allows the exploitation of topological transport properties in narrow ribbons. Using nonequilibrium Green's function calculations, we have examined the electron conductivity upon the presence of Se $\leftrightarrow$ Hg antistructure defects randomly distributed in the Pt_2HgSe_3 scattering region. By considering scattering lengths up to 109 nm, we found localization lengths that can surpass micrometer sizes for narrow nanoribbons ($<$9 nm). These findings can contribute to further understanding the behavior of topological insulators under realistic conditions and their integration within electronic spintronic devices.

DOI: 10.1103/PhysRevB.110.035111

I. INTRODUCTION

Topological insulators (TIs) are an emerging class of intriguing materials with unique electronic properties. Particularly, the wave function that describes their electronic states spans a Hilbert space with a new topology. The consequence is that at any interface, with an ordinary insulator, they will present a gapless state protected by time-reversal symmetry [1].

The first indirect observation of the topological edge states was the measurement of the quantized conductance in HgTe/CdTe quantum wells [2,3]. On the other hand, the direct observation of the electronic state on the surface was possible through an angle-resolved photoemission spectroscopy (ARPES) experiment, first in $Bi_{1-x}Sb_x$ [4]. Despite this, characterizing the surface structure of such materials is not an easy task, and later combined measurements of ARPES, scanning tunneling microscopy (STM), and scanning tunneling spectroscopy (STS) helped to identify TI materials [5,6].

Only a few two-dimensional (2D) materials with the topological helical edge mode showing quantized transport have been measured. For instance, measurements of quantized conductance in the quantum spin Hall geometry have been done in the quantum well systems HgTe/CdTe and InAs/GaSb [2,3,7], on decorated/interfaced graphene [8], and on WTe_2 [9]. STM and STS of edge states in WTe_2 [10,11], at a SiC/bismuthene interface [12], and in jacutingaite mineral (Pt_2HgSe_3) [13] have also been observed. However, those systems were either quantum wells, small gap decorated graphene, and/or 2D materials that were unstable under oxidation [14–16]. This drives a quest to deeply understand their structural and energetic stability: how can intrinsic defects, confinement length (ribbon width), and temperature, to cite a few factors, affect the quantized transport?

Jacutingaite (Pt_2HgSe_3) is a naturally occurring mineral [17] and is stable against oxidation [13]. It gained attention due to the large spin-orbit coupling effect leading to a nontrivial 0.15-eV energy gap opening [18,19], being the first realization of the Kane-Mele topological model [20]. While it is a chemically stable topological insulator, the experimental synthesis of jacutingaite is prone to present defects and disorders. Such effects in the electronic transport of the topological states, combined with confinement potential, bulk density of state, and topological state penetration depth, can change the quantized topological conductance.

In this work, we systematically study the ballistic transport in jacutingaite nanoribbons, including stoichiometric defects, by combining density functional theory (DFT) and electronic transport calculations through nonequilibrium Green's functions. We explore different concentrations of nonmagnetic defects in a disordered geometry and the competition between topological edge-state manifestation and confinement in narrow ribbons. Here we show that the localization length in the transport can surpass micrometer length and allow realistic device engineering in the jacutingaite platform despite the presence of intrinsic defects.

II. METHODOLOGY

A. Equilibrium geometry and electronic structure

To obtain the geometric, energetic, and electronic properties of pristine and defective systems, we performed DFT calculations as implemented in the plane-wave basis Vienna Ab-Initio Simulation Package [21,22]. We employed the semilocal exchange-correlation formalism proposed by

*Contact author: rafael.freire@lnnano.cnpem.br
†Contact author: felipe.lima@ilum.cnpem.br
‡Contact author: hiroki@ufu.br
§Contact author: adalberto.fazzio@ilum.cnpem.br

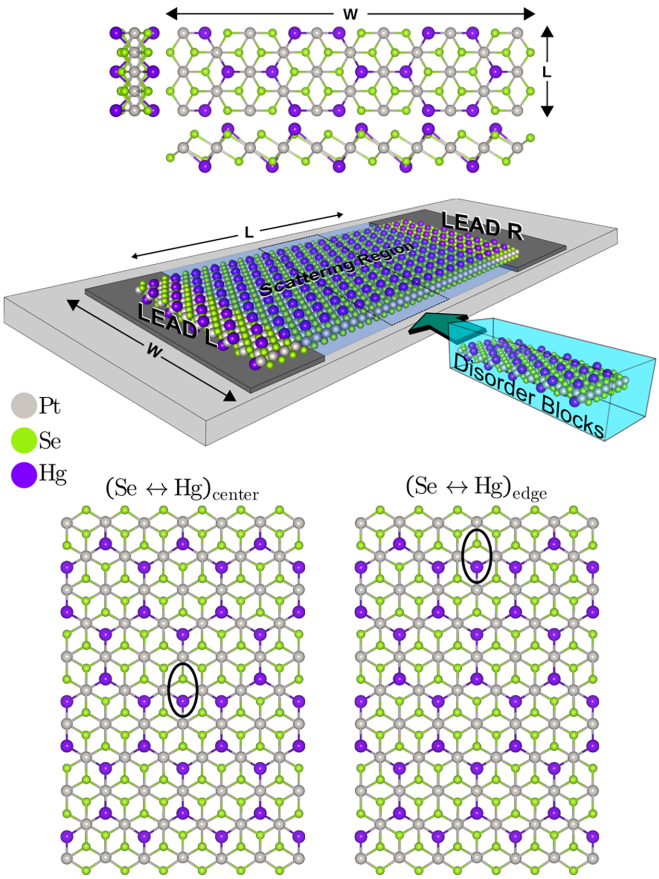

FIG. 1. (Top) Nanoribbon dimensions and illustrative device for electronic transport measurement. (Bottom) Defective building blocks indicating center and edge antistructure defects. Gray, purple, and green atoms represent Pt, Hg, and Se atoms, respectively.

Perdew, Burke, and Ernzerhof (PBE) [23,24]. To improve the description of van der Waals interactions, we used the DFT-D3 pairwise corrections proposed by Grimme [25]. The plane-wave basis energy cutoff was set to 400 eV for all calculations with an energy convergence parameter of 10^{-6} eV, and atoms were allowed to relax until all forces were smaller than 10^{-3} eV/Å. The electron-ion core interactions were described through the projected augmented-wave potentials [26,27]. We integrated the Brillouin zone through a $4 \times 4 \times 1$ k-point mesh for relaxation. We further included relativistic effects by considering spin-orbit coupling corrections (SOC).

B. Electronic transport

In Fig. 1, we present the setup used for the electronic transport calculation. We have considered the Se-terminated zigzag nanoribbons (NRs) [13] where the electronic transport takes place along the z direction, and three NR widths (W) of 34, 60, and 99 Å, parallel to the x direction. We have combined DFT and a recursive Green's function (RGF) method [28]. The system can be decomposed into three main parts, two semi-infinite charge reservoirs, that are the (i) left and (ii) right electrodes, and (iii) the central scattering region. Besides, within the RGF the scattering region can be further split into several building blocks (Disorder Blocks in Fig. 1).

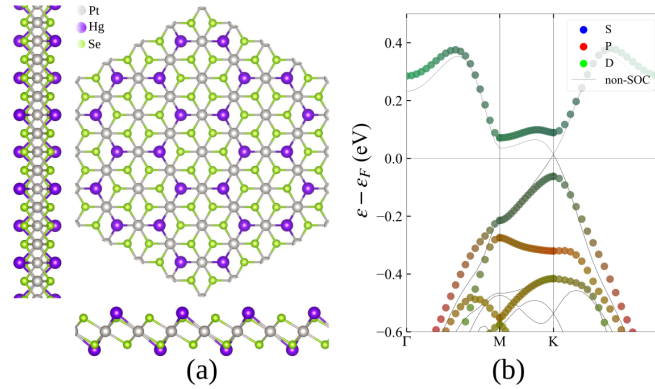

FIG. 2. (a) Jacutingaite monolayer top and side views and (b) electronic band structure with and without SOC effects. Gray, purple, and green atoms represent Pt, Hg, and Se atoms, respectively.

Two distinct building block kinds have been examined, as shown in Fig. 1 (bottom), one with the antistructure defect located in the NR's central region and the other with the defect close to the NR's edge sites. The concatenation of these blocks along the transport direction is random, resulting in scattering lengths (L) up to 0.1 μm. It is also important to note that the blocks were constructed to ensure coupling only between adjacent neighbors. We first obtained the electrodes and scattering region Hamiltonians for the transport calculations through SIESTA-based DFT calculations. Thus, we employed norm-conserving Troullier-Martins pseudopotentials [29] and a single ζ-polarized (SZP) basis set of numerical atomic orbitals to expand the Kohn-Sham orbitals of the valence electrons. Our real-space mesh cutoff was set to 300 Ry and the Brillouin zone was integrated through a Monkhorst-Pack $1 \times 1 \times 10$ ($1 \times 1 \times 3$) k-point mesh for the electrode (scattering) region. Our SZP basis set calculations agree with our plane-wave-based calculations, thus being sufficient to describe the electronic structure of the system.

III. RESULTS

Although the present study focuses on the topologically protected electronic transport in Pt_2HgSe_3 nanoribbons, we start our investigation by examining key structural and electronic properties of pristine and defective Pt_2HgSe_3 monolayer.

A. Pt_2HgSe_3 monolayer

1. Pristine system

Pt_2HgSe_3 is a naturally occurring lamellar material structurally similar to $PtSe_2$ (sudovikovite mineral), but with 25% of Se replaced by Hg. This 3D system has the $P3\bar{m}1$ space group and has been characterized as a metallic system with dual topology [30,31]. This 3D system is experimentally exfoliable [13], with a calculated exfoliation energy of 0.46 J/m^2 [19]. In the monolayer structure, the Hg atoms in Pt_2HgSe_3 pinpoint a honeycomb structure [purple atoms in Fig. 2(a)] embedded in a PtSe matrix. At the equilibrium geometry, the electronic band structure obtained without the inclusion of the SOC is characterized by a Dirac cone structure crossing

TABLE I. Intrinsic point defects' formation energies.

Defect	E^f (eV)
V_{Se}	5.42
V_{Pt}	6.87
V_{Hg}	0.23
(Se ↔ Hg)	0.79

the Fermi level at the K point [Fig. 2(b)]. Meanwhile, upon including the SOC, we found an energy gap at the Dirac point with the band edges composed mainly of Hg 6*s* orbitals hybridized with Pt 4*d* orbitals. Such behavior is typical of the Kane-Mele model [20] and characterizes the topological phase of jacutingaite [18,19]. The energy gap opened by the spin-orbit coupling in the pristine system is calculated here as 0.13 eV. It is worth pointing out that previous studies considering hybrid functionals and GW calculations predicted higher energy gaps of 0.2 eV [19,32] and 0.5 eV [18]. However, experimental STM measurements at 9 K have estimated the energy gap to be 0.08 ± 0.03 eV [13], closer to the one obtained using the DFT–generalized-gradient-approximation approach.

2. Intrinsic defects

The emergence or suppression of a given topological phase as well as its influence on electronic transport can be dictated by the presence of defects [33–36]. For instance, the trivial → nontrivial QSH transition is mediated by the concentration of selenium vacancies (V_{Se}) in $PtSe_2$ monolayer [35].

Here, we have considered vacancies (V_X, with X = Se, Pt, and Hg) and antistructure (Se ↔ Hg) defects [37] in Pt_2HgSe_3 monolayer. The occurrence rate of these defects can be inferred by the calculation of the formation energy (E^f) [38,39],

$$E^f = E_{\text{pristine}} - E_{\text{defect}} - nE_X, \tag{1}$$

where E_{pristine} and E_{defect} are the total energies of the pristine and the defective Pt_2HgSe_3 monolayer; E_X is the total energy of an isolated atom X, and n is the number of missing atoms. For a single X vacancy, V_X, $n = 1$, while for the antistructure defect, which is stoichiometric, $n = 0$. In the antistructure defects, we have considered antisites, Se_{Hg} and Hg_{Se}, created adjacent to each other. Generally, transition metal vacancy has a larger defect formation energy than the chalcogen vacancy [40], which is also verified here (Table I), as V_{Pt} formation energy is higher than that of V_{Se}. However, the formation energy of both defects is larger compared with that of V_{Hg}, 0.23 eV, followed by the (Se ↔ Hg) antistructure, 0.79 eV.

The stoichiometry of Pt_2HgSe_3 has been conserved in experimentally synthesized jacutingaite samples [13,41]. Meanwhile, naturally occurring samples exhibit Pd doping in the Pt site while maintaining the Hg/Se ratio [17]. These results, combined with the lower formation of the (stoichiometric) antistructure defects, allow us to infer that the Se ↔ Hg interchanged defect is quite likely to be present in Pt_2HgSe_3 [42]. In the sequence, we examine the effect of the local disorder induced by the antistructure defect on the electronic transport properties, mediated by the topologically protected edge states in jacutingaite NRs.

B. Pt_2HgSe_3 nanoribbons: Electronic transport

The transport geometry for the monolayer Pt_2HgSe_3 is presented in Fig. 1. The leads are pristine systems, and the scattering region contains the antistructure defects. We explored (i) different nanoribbon widths (W = 34, 60, and 99 Å), (ii) different antistructure concentrations ($\lambda = 1.9 \times 10^6$ and 4.5×10^6 defects/cm), and (iii) different scattering region lengths (L = 15.6, 31.2, and 109.2 nm).

1. Pristine nanoribbons

First, we analyze the conductance through a defect-free jacutingaite NR. In such a case, the incident wave function is also an eigenstate of the scattering region, thus suppressing scattering processes. In Figs. 3(a)–3(c), we present the electronic band structure and the conductance results (in units of $G_0 = e^2/h$) for different NR widths, W = 34, 60, and 99 Å. The band structure presents the projected contribution of the atomic orbitals from the middle of the ribbon, namely, the bulklike region $|\langle \text{bulk}|n, \vec{k}\rangle|^2$, and the orbitals at the edge $|\langle \text{edge}|n, \vec{k}\rangle|^2$. We can identify two topological edge bands close to the Fermi energy. For W = 34 and 60 Å, we can see a gap opening at the Dirac crossing due to the interedge interaction. In contrast, for W = 90 Å, we find the emergence of a Dirac cone at the Γ point.

As shown in Fig. 3 (right), the energy window ($\Delta\varepsilon$) close to the Fermi level with $G = 2G_0$, due to the edge metallic band, decreases as the NR width increases. That is, for W = 90 Å [Fig. 3(c)], we found $\Delta\varepsilon$ of around 0.13 eV, which is compatible with the topological band gap of the single-layer jacutingaite. Whereas, for W = 34 and 60 Å [Figs. 3(a) and 3(b)], in addition to the energy gap at the Dirac point due to the interedge interactions, $\Delta\varepsilon$ increases to about 0.19 and 0.15 eV, which can be attributed to the confinement potential sparsing the bulklike bands [43].

Since the interedge interactions are mediated by the bulk (inner) states, the penetration length (ℓ) of the edge states is a key quantity in understanding the topologically protected electronic transport along the NR's edge channels. Within the Kane-Mele model, the penetration depth is $\ell \sim at\sqrt{3}/(2\lambda)$, with a being the lattice parameter, t the nearest-neighbor hopping, and λ the spin-orbit strength term. Taking these values from the jacutingaite band structure with $t/6$ being the Dirac band width at the Γ point, the SOC gap at the K point, $E^{\text{K}}_{\text{gap}} = 6\sqrt{3}\lambda$, and $a = 7.5$ Å, we can estimate $\ell = 11.2$ nm. In contrast, in Ref. [18] the authors predicted a penetration depth ($\ell = \hbar v_F/E_{\text{gap}}$) of about 4.7 Å, by using an energy gap E_{gap} of 0.53 eV, larger than that observed experimentally, and a v_F of 3.6×10^5 m/s. Further STM measurements showed a penetration length of ∼5 Å in the Se-terminated zigzag jacutingaite NRs [13].

By projecting the edge-state contribution in real space (Fig. 4), we can explicitly calculate the penetration depth (ℓ) by fitting the wave-function decay as $\Psi_{\text{top}}(x) = \phi(x)e^{-x/\ell}$, where $\phi(x)$ is the planar (yz)-averaged single-particle wave function (near the Γ point) of the metallic band crossing the

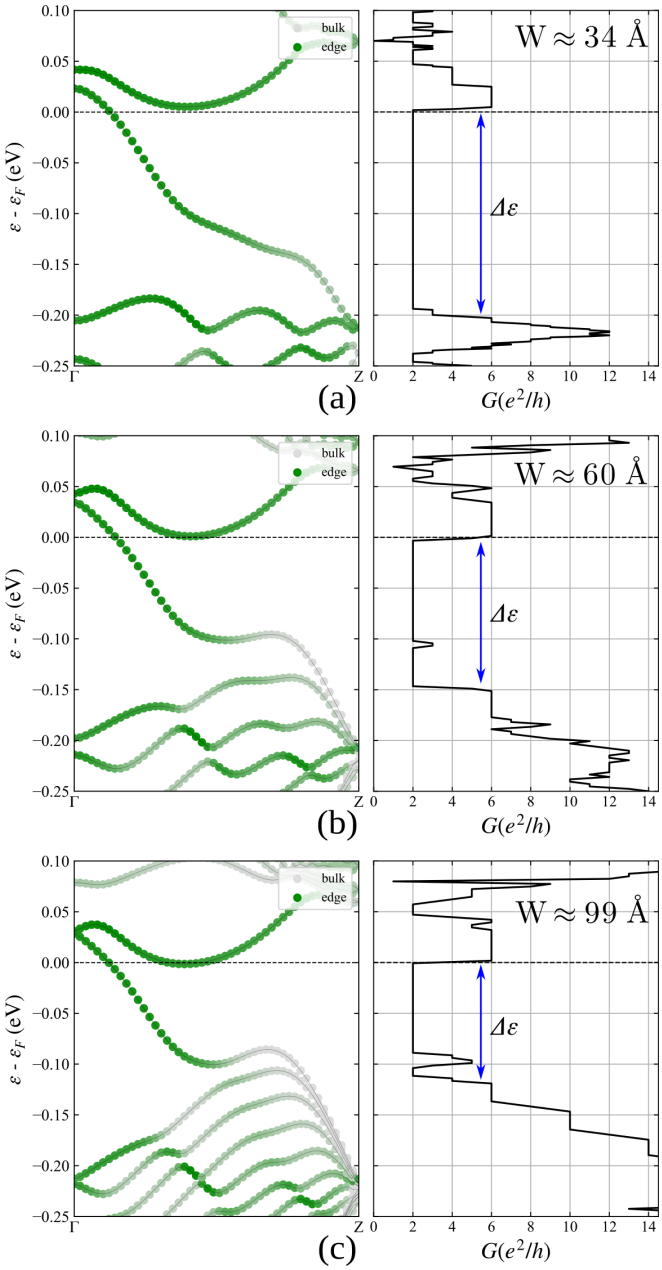

FIG. 3. Electronic band structure projected on the bulk and edge regions (left) and conductance (right) across a Pt_2HgSe_3 nanoribbon with different size widths: (a) $W = 34$ Å, (b) $W = 60$ Å, and (c) $W = 99$ Å. The green and gray colors in the band structure are proportional to the edge ($|\langle \text{edge}|n, \vec{k}\rangle|^2$) and bulk ($|\langle \text{bulk}|n, \vec{k}\rangle|^2$) contributions to the system eigenstate, respectively. For all band structures, each NR edge region for projection is about 7.69 Å wide (perpendicular to transport direction), while the remaining atoms are considered as the bulk projection region.

Fermi level. We found a mean value of $\ell = 0.91$ nm for $W = 34$ and 60 Å [Figs. 4(a) and 4(b)] and $\ell = 0.76$ nm for the widest NR, $W = 99$ Å. It is worth noting that these values of ℓ are lower than predicted considering the empty honeycomb lattice (Kane-Mele model), 11.2 nm, suggesting that the $PtSe_2$ background's dielectric media improves the wave function's screening, and thus reduces the penetration depth. Here it is worth noting that the penetration depth of topological interface states in other systems is reported to be higher. For instance, in HgTe/CdTe quantum wells, it is ∼50 nm [44], and in SmB_6 it is ∼32 nm [45], while in Bi_2Se_3, the 001 (basal plane) surface state has a penetration depth of ∼3 nm [46]. Given the two key points governing the penetration depth discussed in the previous paragraphs, i.e., the spin-orbit strength and the presence of screening media, to find lower penetration depth, we need to look for topological bands with (i) higher spin-orbit coupling strength and (ii) immersion in high-dielectric media. These two points form a design principle for identifying relevant systems.

The reduced penetration depth implies that the topological electronic transport is maintained against interedge scattering processes even in narrow jacutingaite NRs. However, in the case of scattering potentials along the NRs [47,48], we might observe an entirely different picture. In this scenario, the interedge interactions may suppress the electronic transport along the edge channels.

2. *Antistructure defects in NRs*

Here, we study the effect of the scattering potentials induced by the (Se ↔ Hg) antistructure on the electronic transport properties along the jacutingaite NRs. In Figs. 5(a) and 5(b), we present the total charge rearrangement ($\Delta\rho$), defined as the total charge difference between the defective and pristine (defect-free) systems, $\Delta\rho = \rho_{\text{defect}} - \rho_{\text{prist}}$, induced by the antistructure defect at the center and at the edge sites of the NR with $W = 34$ Å. In the former, we see a charge rearrangement with a diameter of ∼0.7 nm, giving the scale of the antistructure defect localization. In contrast, as depicted in Fig. 5(b), an antistructure defect at the edge site of the NR leads to a charge rearrangement at both edges, ruled by the edge-edge coupling present for such a width. Meanwhile, by increasing the ribbon width to $W = 60$ Å [Fig. 5(c)], although both NRs present practically the same penetration length, $\ell = 0.9$ nm [Figs. 4(a) and 4(b)], such a charge density rearrangement at the side opposite to the defect becomes nearly absent. That is, as expected, the interedge interactions are weakened for larger values of NR width concerning the penetration length.

Focusing on the electronic transport properties, using the simulation setup presented in Fig. 1, we calculate the conductance G as a function of the NR width W and length (L). We have considered scattering lengths ranging from 16 up to 109 nm with the antistructure defects randomly distributed along the scattering region, as described in Sec. II B and schematically depicted in Fig. 6(e).

In Figs. 6(a)–6(c), we present our results of conductance in the presence of antistructure defects (G_{defect}, in units of $G_0 = e^2/h$) near the Fermi level, for $W = 34$, 60, and 99 Å and linear concentration of defects (λ) of 4.5×10^6 cm^{-1}. It is noticeable that G_{defect} is smaller than the conductance of the pristine NR (G_{prist}) indicated by dashed lines in Fig. 6. Since the antistructure defects are nonmagnetic, the backscattering process in a single edge is forbidden by the time-reversal symmetry, and thus we can infer that the results of $G_{\text{defect}} < G_{\text{prist}}$ are due to the partial or total interedge backscattering processes within the energy window ($\Delta\varepsilon$ in Fig. 3) of the topological edge states. It is observed that the reduction of

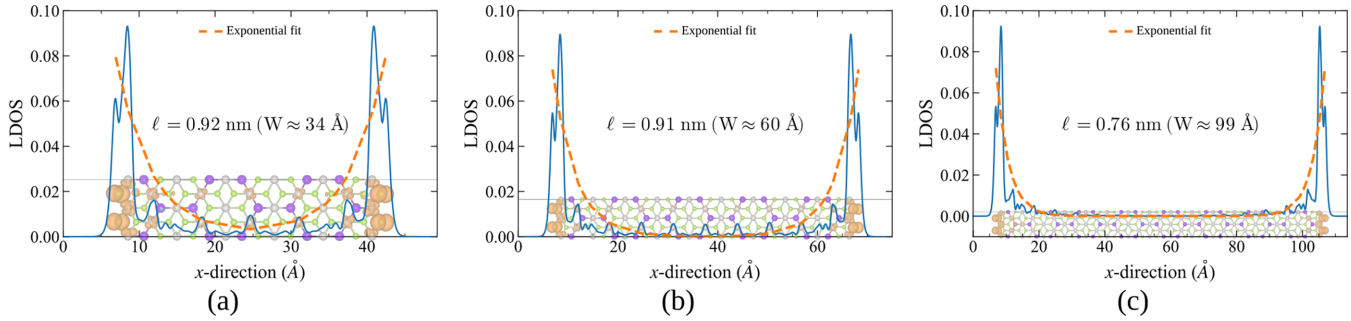

FIG. 4. Penetration depth estimation for different NR widths. Blue curves indicate the planar (yz)-averaged local density of states (LDOS) according to their real-space projection as depicted for each NR width, obeying $|\Psi_{\text{top}}(x)|^2 = |\phi(x)|^2 e^{-2x/\ell}$. Orange dashed lines are the exponential fitting to obtain the respective penetration depth ℓ.

G_{defect} concerning G_{prist} becomes more pronounced, independent of the NR width, for energies below -0.1 eV, i.e., $\varepsilon - \varepsilon_{\text{F}} < -0.1$ eV, suggesting the predominance of the bulk states in the electronic transport along the NR. Furthermore, the following results are noteworthy.

(i) For a given NR width and defect concentration, λ, G_{defect} decreases for higher values of $L = 15.6$–109.2 nm, since the scattering rate increases with the length of the scattering region. Indeed, as shown in Figs. 6(a) and 6(d), by reducing the concentration of the defects, $\lambda = 4.5 \rightarrow 1.9 \times 10^6$ cm^{-1}, we find that the reduction of G_{defect} is mitigated.

(ii) For a given value of λ, the reduction of G_{defect} is also mitigated by increasing the NR's width, $W = 34 \rightarrow 99$ Å [Figs. 6(a)–6(c)]. This can be attributed to the reduction of the interedge backscattering since the ratio between the penetration length of the edge states and the NR width, ℓ/W, reduces for wider systems. For instance, $\ell/W = 0.27$ and 0.08 for $W = 34$ and 99 Å, respectively.

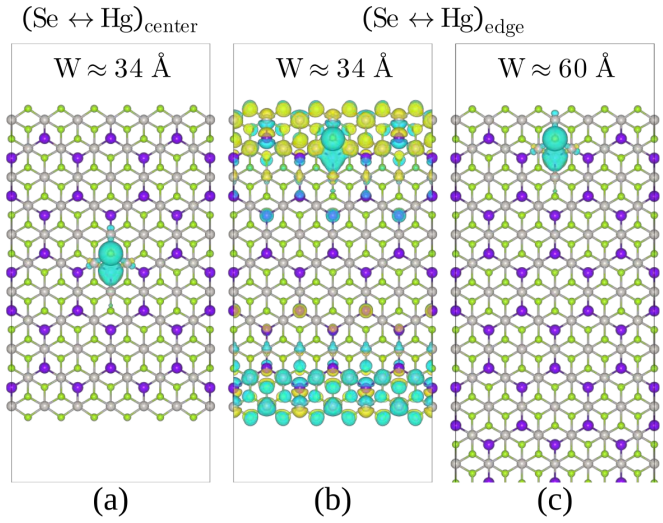

FIG. 5. Charge density difference with/without the defect presence $\Delta\rho(\vec{r}) = \rho_{\text{def}}(\vec{r}) - \rho_{\text{pris}}(\vec{r})$, for the $W = 34$ Å nanoribbon [panels (a) and (b)] and for the $W = 60$ Å nanoribbon [panel (c)]. In panel (a) the defect is located in the center of the ribbon, while in panels (b) and (c) the defect is at the ribbon's edge. Blue (yellow) regions indicate a decrease (increase) in the electron concentration. The isosurface value is 0.01 e Å^{-1}.

The energy dependence of G_{defect} and the width of the NRs [(ii)] reveals that the deviation of G_{defect} for G_{prist} is proportional to the interedge orbital couplings mediated by the antistructure states. In the present study of antistructure defects, we find that $G_{\text{defect}} \approx 2G_0$ for $\varepsilon - \varepsilon_{\text{F}}$ about -0.05 eV, as depicted in Figs. 6(b) and 6(c), thus indicating that the edge-edge interaction is nearly suppressed around 0.05 eV below the Fermi level. Other (nonmagnetic) defects may result in different energy intervals where the interedge coupling is minimized. On the other hand, in the limit of $W \rightarrow \infty$, perfect conducting channels with $G_{\text{defect}} = G_{\text{prist}}$ should be observed, independent of the scattering region length and the concentration of the defects. Given the discussed robustness of narrow ribbons, it is worth highlighting that possible external factors such as temperature, at ambient conditions (25 meV), would introduce electronic characteristics lower than the topological gap (130 meV), which we expect to maintain the topological character. Additionally, constructing an interface could allow for possible control over the topological states through a gate voltage.

3. Localization length

Given the random distribution of the scattering potential, induced by the antistructure defects here, at first glance, our conductance results can be interpreted in terms of Anderson localization. In this case, we can gain further insights by looking into the localization length ξ as a function of the energy, where ξ is defined as the length in which the conductance decays by an exponential factor [49,50],

$$G = G_0 e^{-L/\xi}, \tag{2}$$

where G_0 is an exponential prefactor, and L is the length of scattering region. From the last equation, we can have

$$\ln(G/G_0) = -\frac{L}{\xi}. \tag{3}$$

Within this model, ξ is inversely proportional to the density of the scattering centers, ρ, namely $\xi \propto \rho^{-1}$ [50]. Thus, a given material's NR with the same defect concentration is expected to present similar localization lengths. However, this is not what we found in our systems. Instead, ξ presents an NR's width dependence due to (i) the interedge scattering process of the topological states and (ii) the distinct behavior

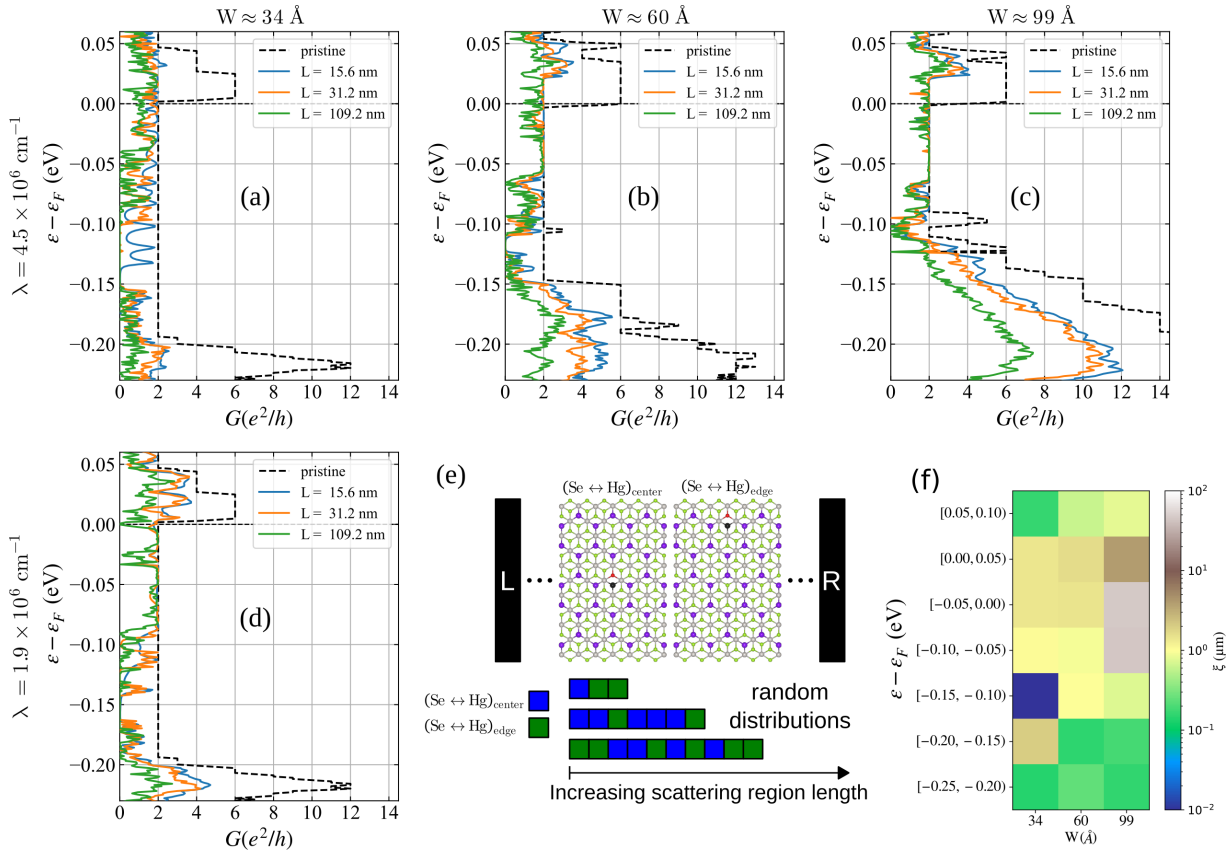

FIG. 6. Conductance as a function of nanoribbon length for the defect scattering region: (a)–(c) for a linear defect concentration of $\lambda = 4.5 \times 10^6$ cm^{-1} and (d) for $\lambda = 1.9 \times 10^6$ cm^{-1}. In panels (a) and (d), the ribbons have width $W = 34$ Å; in panel (b), $W = 60$ Å; and in panel (c), $W = 99$ Å. In panel (e), we schematically present the distribution of the defects as a function of the ribbon length. (f) The average localization length ξ for different energy ranges and nanoribbon with W for $\lambda = 4.5 \times 10^6$ cm^{-1}.

of the electronic transport through the bulk and edge channels, where the latter (former) is (is not) topologically protected.

The behavior of G vs L is presented in Fig. 6 where we estimated the localization lengths. Given the random distribution of defects for each L an oscillation of G/G_0 for each energy is expected, driven by the defect-defect interaction. However, across energy ranges wider than the defect-defect interaction, a mean localization length remains robust. In Fig. 6(f) we present average values of ξ for energy ranges with a 0.05-eV window. For energies outside the topological edge-state range $\varepsilon - \varepsilon_F < -0.1$ we see a localization length of 10^{-1} μm, that is the localization of the system trivial bulk-like states. Within the topological gap $0.05 > \varepsilon - \varepsilon_F > -0.1$, the localization length increases compared to those on the bulk-like energy range; that is, the backscattering forbidden topological transport is dominant. Additionally, within the topological edge-state energy range there is an increase in the localization length concerning the ribbon width W reaching up to 10^1 μm for $W = 99$ Å at the Fermi energy, $\varepsilon - \varepsilon_F = 0$. Despite that for narrow ribbons ($W = 34$ Å) the nonmagnetic impurity leads to edge-to-edge scattering, there exist energy ranges that can preserve long-range transport with conductance $2G_0$, for instance, for $\varepsilon - \varepsilon_F = -0.05$ eV below the Fermi energy, reaching localization length up to ~ 6 μm. Thus, regardless of intrinsic defects, the Pt_2HgSe_3 platform allows the exploitation of topological states in narrow ribbons.

IV. CONCLUSIONS

We investigated the electronic transport properties of 2D jacutingaite nanoribbons including defects and disorders within the systems. We analyzed the electronic conductance for different-width nanoribbons and different device lengths along the transport direction. Our *ab initio* results indicate a synergy between the confinement potential and manifestation of topological edge states that increase the energy range associated with the topological edge states in narrow ribbons. Stoichiometric defects in this system have a spatial length of $\sim$0.7 nm, while the edge-state penetration depth, $\sim$0.9 nm, is much lower than in other 2D topological systems. By considering scattering lengths up to 109 nm, we found localization lengths that can surpass micrometer sizes for narrow nanoribbons (<9 nm). This allows the exploitation of topological transport properties in narrow ribbons. In fact, by computing the transport localization length we show that a topologically driven transport can survive high defect densities of $\sim 10^6$ cm^{-1} for ribbons with width $W = 34$ Å. Our analysis can contribute to the fundamental understanding and design integration of TIs within spintronic devices.

ACKNOWLEDGMENTS

The authors acknowledge financial support from the Brazilian agencies FAPESP (Grants No. 20/14067-3, No. 19/20857-0, and No. 17/02317-2), FAPEMIG, CNPq, INCT-Nanocarbono, INCT-Materials Informatics (Grant No. 167651/2023-4), and Laboratório Nacional de Computação Científica for computer time (Projects ScafMat2 and emt2D).

There are no conflicts of interest to declare.

[1] M. Z. Hasan and C. L. Kane, *Colloquium:* Topological insulators, Rev. Mod. Phys. **82**, 3045 (2010).

[2] M. König, S. Wiedmann, C. Brüne, A. Roth, H. Buhmann, L. W. Molenkamp, X.-L. Qi, and S.-C. Zhang, Quantum spin Hall insulator state in HgTe quantum wells, Science **318**, 766 (2007).

[3] A. Roth, C. Brüne, H. Buhmann, L. W. Molenkamp, J. Maciejko, X.-L. Qi, and S.-C. Zhang, Nonlocal transport in the quantum spin Hall state, Science **325**, 294 (2009).

[4] D. Hsieh, D. Qian, L. Wray, Y. Xia, Y. S. Hor, R. J. Cava, and M. Z. Hasan, A topological Dirac insulator in a quantum spin Hall phase, Nature (London) **452**, 970 (2008).

[5] Z. Alpichshev, J. G. Analytis, J.-H. Chu, I. R. Fisher, Y. L. Chen, Z. X. Shen, A. Fang, and A. Kapitulnik, STM imaging of electronic waves on the surface of Bi_2Te_3: Topologically protected surface states and hexagonal warping effects, Phys. Rev. Lett. **104**, 016401 (2010).

[6] K. L. Wang, M. Lang, and X. Kou, Spintronics of topological insulators, in *Handbook of Spintronics* (Springer, Dordrecht, Netherlands, 2016), pp. 431–462.

[7] L. Du, I. Knez, G. Sullivan, and R.-R. Du, Robust helical edge transport in gated InAs/GaSb bilayers, Phys. Rev. Lett. **114**, 096802 (2015).

[8] K. Hatsuda, H. Mine, T. Nakamura, J. Li, R. Wu, S. Katsumoto, and J. Haruyama, Evidence for a quantum spin Hall phase in graphene decorated with Bi_2Te_3 nanoparticles, Sci. Adv. **4**, eaau6915 (2018).

[9] S. Wu, V. Fatemi, Q. D. Gibson, K. Watanabe, T. Taniguchi, R. J. Cava, and P. Jarillo-Herrero, Observation of the quantum spin Hall effect up to 100 Kelvin in a monolayer crystal, Science **359**, 76 (2018).

[10] S. Tang, C. Zhang, D. Wong, Z. Pedramrazi, H.-Z. Tsai, C. Jia, B. Moritz, M. Claassen, H. Ryu, S. Kahn, J. Jiang, H. Yan, M. Hashimoto, D. Lu, R. G. Moore, C.-C. Hwang, C. Hwang, Z. Hussain, Y. Chen, M. M. Ugeda *et al.*, Quantum spin Hall state in monolayer 1T'-WTe_2, Nat. Phys. **13**, 683 (2017).

[11] P. Chen, W. W. Pai, Y.-H. Chan, W.-L. Sun, C.-Z. Xu, D.-S. Lin, M. Y. Chou, A.-V. Fedorov, and T.-C. Chiang, Large quantum-spin-Hall gap in single-layer 1T' WSe_2, Nat. Commun. **9**, 2003 (2018).

[12] F. Reis, G. Li, L. Dudy, M. Bauernfeind, S. Glass, W. Hanke, R. Thomale, J. Schäfer, and R. Claessen, Bismuthene on a SiC substrate: A candidate for a high-temperature quantum spin Hall material, Science **357**, 287 (2017).

[13] K. Kandrai, P. Vancsó, G. Kukucska, J. Koltai, G. Baranka, A. Hoffmann, A. Pekker, K. Kamarás, Z. E. Horváth, A. Vymazalová, L. Tapasztó, and P. Nemes-Incze, Signature of large-gap quantum spin Hall state in the layered mineral jacutingaite, Nano Lett. **20**, 5207 (2020).

[14] F. Ye, J. Lee, J. Hu, Z. Mao, J. Wei, and P. X. Feng, Environmental instability and degradation of single- and few-layer WTe_2 nanosheets in ambient conditions, Small **12**, 5802 (2016).

[15] C. H. Naylor, W. M. Parkin, Z. Gao, H. Kang, M. Noyan, R. B. Wexler, L. Z. Tan, Y. Kim, C. E. Kehayias, F. Streller, Y. R. Zhou, R. Carpick, Z. Luo, Y. W. Park, A. M. Rappe, M. Drndi, J. M. Kikkawa, and A. T. C. Johnson, Large-area synthesis of high-quality monolayer 1T'-WTe_2 flakes, 2D Mater. **4**, 021008 (2017).

[16] R. L. H. Freire, F. C. de Lima, and A. Fazzio, Substrate suppression of oxidation process in pnictogen monolayers, Phys. Chem. Chem. Phys. **26**, 9149 (2024).

[17] A. R. Cabral, H. F. Galbiatti, R. Kwitko-Ribeiro, and B. Lehmann, Platinum enrichment at low temperatures and related microstructures, with examples of hongshiite (PtCu) and empirical 'Pt_2HgSe_3' from Itabira, Minas Gerais, Brazil, Terra Nova **20**, 32 (2008).

[18] A. Marrazzo, M. Gibertini, D. Campi, N. Mounet, and N. Marzari, Prediction of a large-gap and switchable Kane-Mele quantum spin Hall insulator, Phys. Rev. Lett. **120**, 117701 (2018).

[19] F. C. de Lima, R. H. Miwa, and A. Fazzio, Jacutingaite-family: A class of topological materials, Phys. Rev. B **102**, 235153 (2020).

[20] C. L. Kane and E. J. Mele, Quantum spin Hall effect in graphene, Phys. Rev. Lett. **95**, 226801 (2005).

[21] G. Kresse and J. Hafner, *Ab initio* molecular dynamics for open-shell transition metals, Phys. Rev. B **48**, 13115 (1993).

[22] G. Kresse and J. Furthmüller, Efficient iterative schemes for *ab initio* total-energy calculations using a plane-wave basis set, Phys. Rev. B **54**, 11169 (1996).

[23] J. P. Perdew, K. Burke, and M. Ernzerhof, Generalized gradient approximation made simple, Phys. Rev. Lett. **77**, 3865 (1996).

[24] J. P. Perdew, K. Burke, and M. Ernzerhof, Generalized gradient approximation made simple [Phys. Rev. Lett. **77**, 3865 (1996)] Phys. Rev. Lett. **78**, 1396(E) (1997).

[25] S. Grimme, J. Antony, S. Ehrlich, and H. Krieg, A consistent and accurate *ab initio* parametrization of density functional dispersion correction (DFT-D) for the 94 elements H-Pu, J. Chem. Phys. **132**, 154104 (2010).

[26] P. E. Blöchl, Projector augmented-wave method, Phys. Rev. B **50**, 17953 (1994).

[27] G. Kresse and D. Joubert, From ultrasoft pseudopotentials to the projector augmented-wave method, Phys. Rev. B **59**, 1758 (1999).

[28] A. R. Rocha, M. Rossi, A. Fazzio, and A. J. R. da Silva, Designing real nanotube-based gas sensors, Phys. Rev. Lett. **100**, 176803 (2008).

[29] N. Troullier and J. L. Martins, Efficient pseudopotentials for plane-wave calculations, Phys. Rev. B **43**, 1993 (1991).

[30] I. Cucchi, A. Marrazzo, E. Cappelli, S. Riccò, F. Y. Bruno, S. Lisi, M. Hoesch, T. K. Kim, C. Cacho, C. Besnard, E.

Giannini, N. Marzari, M. Gibertini, F. Baumberger, and A. Tamai, Bulk and surface electronic structure of the dual-topology semimetal Pt_2HgSe_3, Phys. Rev. Lett. **124**, 106402 (2020).

[31] A. Marrazzo, N. Marzari, and M. Gibertini, Emergent dual topology in the three-dimensional Kane-Mele Pt_2HgSe_3, Phys. Rev. Res. **2**, 012063(R) (2020).

[32] X. Wu, M. Fink, W. Hanke, R. Thomale, and D. Di Sante, Unconventional superconductivity in a doped quantum spin Hall insulator, Phys. Rev. B **100**, 041117(R) (2019).

[33] F. Lüpke, M. Eschbach, T. Heider, M. Lanius, P. Schüffelgen, D. Rosenbach, N. von den Driesch, V. Cherepanov, G. Mussler, L. Plucinski, D. Grützmacher, C. M. Schneider, and B. Voigtländer, Electrical resistance of individual defects at a topological insulator surface, Nat. Commun. **8**, 15704 (2017).

[34] N. Fukui, R. Hobara, A. Takayama, R. Akiyama, T. Hirahara, and S. Hasegawa, Scattering of topological surface-state carriers at steps on surfaces, Phys. Rev. B **102**, 115418 (2020).

[35] F. Crasto de Lima and A. Fazzio, At the verge of topology: Vacancy-driven quantum spin Hall in trivial insulators, Nano Lett. **21**, 9398 (2021).

[36] A. Pezo, F. C. de Lima, and A. Fazzio, Electronic and spin transport in bismuthene with magnetic impurities, Solid State Commun. **376**, 115358 (2023).

[37] A. Janotti, A. Fazzio, P. Piquini, and R. Mota, Defect complexes in GaAs: First-principles calculations, Phys. Rev. B **56**, 13073 (1997).

[38] H.-P. Komsa, J. Kotakoski, S. Kurasch, O. Lehtinen, U. Kaiser, and A. V. Krasheninnikov, Two-dimensional transition metal dichalcogenides under electron irradiation: Defect production and doping, Phys. Rev. Lett. **109**, 035503 (2012).

[39] J. Chen, J. Zhou, W. Xu, Y. Wen, Y. Liu, and J. H. Warner, Atomic-level dynamics of point vacancies and the induced stretched defects in 2D monolayer $PtSe_2$, Nano Lett. **22**, 3289 (2022).

[40] R. L. H. Freire, F. C. de Lima, and A. Fazzio, Vacancy localization effects on MX_2 transition-metal dichalcogenides: A systematic *ab initio* study, Phys. Rev. Mater. **6**, 084002 (2022).

[41] A. Vymazalova, F. Laufek, M. Drabek, A. R. Cabral, J. Haloda, T. Sidorinova, B. Lehmann, H. F. Galbiatti, and J. Drahokoupil, Jacutingaite, Pt_2HgSe_3, a new platinum-group mineral species from the Caue iron-ore deposit, Itabira District, Minas Gerais, Brazil, Can. Mineral. **50**, 431 (2012).

[42] F. Crasto de Lima, B. Focassio, R. H. Miwa, and A. Fazzio, Topological insulating phase arising in transition metal dichalcogenide alloy, 2D Mater. **10**, 035001 (2023).

[43] Y.-W. Son, M. L. Cohen, and S. G. Louie, Energy gaps in graphene nanoribbons, Phys. Rev. Lett. **97**, 216803 (2006).

[44] B. Zhou, H.-Z. Lu, R.-L. Chu, S.-Q. Shen, and Q. Niu, Finite size effects on helical edge states in a quantum spin-Hall system, Phys. Rev. Lett. **101**, 246807 (2008).

[45] T. Liu, Y. Li, L. Gu, J. Ding, H. Chang, P. A. P. Janantha, B. Kalinikos, V. Novosad, A. Hoffmann, R. Wu, C. L. Chien, and M. Wu, Nontrivial nature and penetration depth of topological surface states in SmB_6 thin films, Phys. Rev. Lett. **120**, 207206 (2018).

[46] Z. Wang, T. Zhou, T. Jiang, H. Sun, Y. Zang, Y. Gong, J. Zhang, M. Tong, X. Xie, Q. Liu, C. Chen, K. He, and Q.-K. Xue, Dimensional crossover and topological nature of the thin films of a three-dimensional topological insulator by band gap engineering, Nano Lett. **19**, 4627 (2019).

[47] M. König, M. Baenninger, A. G. F. Garcia, N. Harjee, B. L. Pruitt, C. Ames, P. Leubner, C. Brüne, H. Buhmann, L. W. Molenkamp, and D. Goldhaber-Gordon, Spatially resolved study of backscattering in the quantum spin Hall state, Phys. Rev. X **3**, 021003 (2013).

[48] S. Essert and K. Richter, Magnetotransport in disordered two-dimensional topological insulators: Signatures of charge puddles, 2D Mater. **2**, 024005 (2015).

[49] B. Kramer and A. MacKinnon, Localization: Theory and experiment, Rep. Prog. Phys. **56**, 1469 (1993).

[50] A. R. Rocha, T. B. Martins, A. Fazzio, and A. J. R. Silva, Disorder-based graphene spintronics, Nanotechnology **21**, 345202 (2010).